

Understanding phonon selection and interference in momentum-resolved electron energy loss spectroscopy

Thomas W. Pfeifer*

*Department of Mechanical and Aerospace Engineering,
University of Virginia, Charlottesville, Virginia 22920, USA*

Harrison A. Walker and Sokrates Pantelides

*Department of Interdisciplinary Materials Science,
Vanderbilt University, Nashville, Tennessee 37235, USA*

Henry Aller and Samuel Graham

Department of Mechanical Engineering, University of Maryland, College Park, Maryland 20742, USA

Jordan A. Hachtel and Eric R. Hoglund†

Center for Nanophase Materials Sciences, Oak Ridge National Laboratory, Oak Ridge, Tennessee 37830, USA

Patrick E. Hopkins‡

*Department of Mechanical and Aerospace Engineering,
University of Virginia, Charlottesville, Virginia 22920, USA*

Department of Physics, University of Virginia, Charlottesville, Virginia 22920, USA and

*Department of Materials Science and Engineering,
University of Virginia, Charlottesville, Virginia 22920, USA*

(Dated: March 14, 2025)

As momentum-resolved Electron Energy Loss Spectroscopy (q-EELS) becomes more widely used for phonon measurements, better understanding of the intricacies of the acquired signal becomes necessary. Selection rules limit the allowed scattering directions, which may prohibit the appearance of specific phonon branches, and features may appear with no clear explanation. To explore both, we perform frequency-resolved q-EELS simulations via the multislice method and compare results to Spectral Energy Density (SED) and Lattice Dynamics (LD) calculations. We discuss common misconceptions of phonon behavior and characterization generally and in the context of measured or simulated q-EELS signals. We highlight the presence of an “interferometric Brillouin zone” (closely related to the Dynamic Structure Factor), resulting from the simultaneous sampling of the lattice across each basis index. We also demonstrate the scattering selection rules on well-studied systems and explore the acquisition of a polarization-selective signal based on this phenomena. Finally, we identify thickness-dependent sensitivity effects, where the upper surface of a film is sampled at a disproportionate level. We show that this can yield sensitivity to through-plane vibrational modes, which may be measured experimentally assuming sufficient sensitivity can be achieved. Our work should serve as a road map to guide momentum-resolved vibrational EELS measurements in the future, particularly as ever-increasing energy and momentum resolution becomes available.

INTRODUCTION

The advent of high energy resolution in Electron Energy Loss Spectroscopy (EELS) has enabled measurements of phonon spectra in the electron microscope. This relatively recent development allows for EELS measurements at high spatial and/or momentum resolution, making the technique promising for a range of applications, including topologically isolated phonons, chiral phonons, as well as measurements in low-symmetry directions, with applications in phonon engineering. Recent works have developed the computational tools for simulating these experiments [1, 2]. Several aspects of the measured or simulated signals remain to be addressed however. For example, selection rules [3] may prohibit the appearance of certain phonon branches. These phenomena exist separately from issues of instrument resolution

or sensitivity. Similarly, the ability to measure a localized polarization-dependent vibrational density of states (v-DOS) can lend insights into material and vibrational properties [4–6], but a thorough understanding of the vibrational momentum-resolved EELS (q-EELS) signal is required.

In this work, we seek a thorough explanation of all features in q-EELS signals by performing simulations in a manner similar to Zeiger [1] and Castellanos-Reyes [2], and compare results to Spectral Energy Density (SED) [7] and Lattice Dynamics (LD) calculations. These simulations and comparisons allow differentiation between effects due to the fundamental behavior of phonons versus those related to the fast-electron phonon scattering interactions. We explore two popular and commercially-relevant material systems: silicon, and aluminum nitride (AlN). Silicon is well-studied and its face-center-cubic

crystal lattice is highly symmetric, reducing the number of reciprocal directions required for analysis and simplifying the simulations. Conversely, AlN has the highly anisotropic wurtzite crystal structure, enabling exploration of some of the direction-selectivity behavior of q-EELS. We believe this work will serve as a roadmap to guide future momentum-resolved vibrational EELS measurements, particularly as ever increasing energy and momentum resolution becomes available.

METHODS

Momentum-Resolved EELS calculations

Our q-EELS simulations are performed in a manner similar to that of Zeiger [1] and Castellanos-Reyes [2]. In either case, molecular dynamics (MD) simulations are used to acquire time-dependent atomic configurations, which are then used as the input for frozen phonon multislice (electron wave propagation) simulations. While the electron wave simulations are elastic (no energy loss is simulated), the result contains information on the frequency-dependent vibrations from MD and the scattering probabilities of the transmitted electrons [8].

Two slightly differing methods for these simulations have been developed, the first of which was by Zeiger *et al.* [1]. Given the frequency-resolved nature of these simulations and the use of multislice simulations for the electron wave, they have been referred to as “Frequency-Resolved Frozen-Phonon Multislice” or “FRFPMS”. These simulations originally made use of a custom frequency-specific thermostat to generate atomic configuration snapshots corresponding to a given frequency, however subsequent works simply use a band-pass filter over a single MD simulation. The resulting frequency-filtered atomic configurations are then used for frozen phonon multislice simulations. The q-EELS signal for a given energy bin is then obtained by taking the difference between the incoherent and coherent sum across multiple frozen phonon configurations.

In the work of Castellanos-Reyes *et al.* [2], multislice simulations are performed over consecutive timesteps, and a Fourier transform over time yields the energy-resolved q-EELS signal. The Fourier transform over the multislice exit wave is referred to as the “time autocorrelation of the auxiliary wave” and this approach has thus been referred to as the “TACAW” method. TACAW yields similar results to FRFPMS, but it is much more computationally efficient. FRFPMS requires multiple frozen phonon configurations for each energy (where parameters such as convergence-angle and sample thickness affect the number of configurations required). By comparison, the number of time-steps used in TACAW directly translates to the frequency resolution.

In this work, we use the TACAW method (the post-hoc

Fourier transform approach developed by Castellanos-Reyes *et al.* [2]). We also performed simulations using FRFPMS (the frequency-binning method developed by Zeiger *et al.* [1]) to ensure observations were maintained (an example is available in the Supplemental Material). We use the Large-scale Atomic/Molecular Massively Parallel Simulator software (LAMMPS [9]) for our molecular dynamics (MD) simulations, and abTEM [10] for our multislice simulations. None of our findings should be unique to the simulation method (“FRFPMS” vs. “TACAW”), or the software packages used (LAMMPS, or abTEM). We will thus refer to the combined molecular dynamics and frequency-resolved elastic multislice simulations as “q-EELS simulations”, as the precise method or software should not affect the overall results.

Our q-EELS simulations begin with molecular dynamics (MD), with the velocities and displacements exported at frequent intervals (chosen based on the maximum phonon frequency expected within the system). All of our MD is performed under the NVE ensemble at room temperature with periodic boundary conditions. Periodic boundary conditions do not imply that an infinite volume is simulated however, as the length of the system constrains what modes are present. For a crystal with N atoms along a given direction, there are N modes along each branch within the first Brillouin zone. Simulation sizes are therefore selected based on a balance of reciprocal space resolution (favoring larger simulations) and computational abilities (limiting the maximum volume being simulated). Details on the exact simulations will be listed in subsequent sections. The suitability of the periodic boundaries in the through-plane direction will also be discussed.

Multislice simulations are then performed over the atomic configuration for each timestep. The multislice exit waves (containing all elastic electron scattering information) are recorded in reciprocal space. Exit waves can be recorded as a function of depth through the sample, meaning the result of the simulation is a 3D or 4D data cube with axes of ω , k_x , k_y and optionally z . Post-processing of this data cube depends on the analysis one is interested in. A phonon dispersion can be found by taking a slice along an arbitrary reciprocal vector (yielding an intensity distribution as a function of ω and k). Slices can be taken at a fixed ω , yielding what is effectively a phonon iso-energy surface in reciprocal space (or an energy-resolved diffraction image). Alternatively, a portion of reciprocal space can be incoherently summed to yield a single spectrum corresponding to the momentum-projected v-DOS. This v-DOS can also be evaluated as a function of thickness. Code for these simulations is available in the abEELS GitHub and is linked in the Supplementary Material.

Spectral Energy Density and Dynamic Structure Factor

Spectral Energy Density (SED) calculations were developed as a means of analyzing the wavevector (k) of collective vibrations that are present within a molecular dynamics (MD) simulation. In this work, we use a variation on SED to compare and understand observations from the vibrational q-EELS simulations, as SED captures the phonons that are present within the MD system (including at finite temperature) without the effects of electron scattering behavior. In the original works of Thomas *et. al.* [7], SED is presented as:

$$\Phi(\omega, k) = \frac{1}{4\pi\omega_f N_T} \sum_{\alpha} \sum_j^B \left| \int_0^{\omega_f} \sum_n^N v_{\alpha,n,j}(t) \cdot \exp[i \cdot k \cdot \bar{r}_{\beta,n,j=0} - i \cdot \omega \cdot t] dt \right|^2, \quad (1)$$

where index pairs n and j denote an atom in the n^{th} primitive unit cell for the j^{th} atom in the basis. The velocity of an atom at each timestep is thus $v_{\alpha,n,j}(t)$, in a given direction α . $\bar{r}_{\beta,n,j=0}$ denotes the time-averaged position of the atom's unit cell (n , for $j=0$) in a given direction (β corresponding to a given Brillouin zone direction). The expression above is effectively coherent summing across unit cells (over all atoms sharing a given basis index j), and incoherent summing across atoms within the basis (and polarizations, which is the direction of atomic displacements α).

This, along with the use of the unit cell position $\bar{r}_{\beta,n,b=0}$ as opposed to the atom position $\bar{r}_{\beta,n,b}$, is required to reproduce the expected phonon dispersion for systems with a basis of more than one atom. For a crystal with multiple atoms in the primitive cell, optical modes are present, in which alternating atoms vibrate out of phase with respect to each other. Phonons are typically analyzed on the unit-cell basis, with a separate eigenvector (a complex 3D vector denoting vibrational displacements) calculated for each atomic basis index. In some cases, an alternate description of a given mode can be found, with a wavelength shorter than the unit cell (but longer than the interatomic spacing), applied to every atom within the system (as opposed to only atoms on a given basis index). This shorter wavelength equates to a higher k in higher-order Brillouin zones, and appears as an “unfolding” of portions of the phonon dispersion across the Brillouin zone boundary. Using the unit cell origin position ($\bar{r}_{\beta,n,b=0}$) as opposed to each atom's position ($\bar{r}_{\beta,n,b}$) means that the folded state is captured (as the phase of the wave is offset by wavevector k).

To emulate an experiment where every atom is sampled (or the phase of atomic bases is allowed to destructively interfere), we can simplify the analysis by ignoring the

basis and considering the atom's average positions. This is expressed as:

$$\Phi(\omega, k) = \sum_{\alpha} \left| \int_0^{\omega_f} \sum_n^N v_{\alpha}(n, t) \cdot e^{i \cdot k \cdot \bar{r}_{\beta,n} - i \cdot \omega \cdot t} dt \right|^2, \quad (2)$$

where n is simply the atom ID and $\bar{r}_{\beta,n}$ is the atom's time-averaged position in a given direction. This can be understood as simply a discrete Fourier transform in space ($X_k = \sum_{n=0}^N x_n \cdot e^{-i \cdot k \cdot n}$) and a continuous Fourier transform in time ($F(\omega) = \int_{-\infty}^{\infty} f(t) \cdot e^{-i \cdot \omega \cdot t} dt$), which describes the plane-wave solutions for the motion of atoms: $u(t, x) = e^{i \cdot (\omega \cdot t - k \cdot x)}$.

A key aspect of this change is that the sum over the basis indices is now part of a coherent sum, allowing interference of waves between bases. Incoherently summing across bases yields the traditional phonon dispersion, while coherent summing across all atoms yields an apparent unfolding of the dispersion. In this work, we will refer to this unfolded Brillouin zone as the “interferometric Brillouin zone”, since it appears as a new larger minimum repeating area in reciprocal space due to interference effects. The size of this larger interferometric Brillouin zone is then tied to the minimum interatomic spacing in the direction of interest (rather than the primitive cell size), which defines the minimum wavelengths that can be sampled. Examples of this will be shown in later sections.

It should be noted that our simplified expression for SED is functionally identical to the Dynamic Structure Factor (DSF) commonly seen in inelastic electron, x-ray, and neutron scattering experiments for specific assumptions [11]. The expressions are mathematically identical under the Born approximation, for harmonic crystals [12], with one-phonon interactions (a full mathematical comparison is shown in the Supplemental Material). While SED is simply a direct measure of phonons in the system, the Born approximation and Van Hove correlation function [13] suggest that the scattering of particles (which do not meaningfully alter the scatterer populations) simply depends on the population that is present. For the one-phonon interaction case, scattering of the electron directly matches the population, as multiple-scattering events are not considered.

When comparing SED to q-EELS simulations, it should be noted that q-EELS is sensitive to atomic displacements as opposed to velocities. For a direct comparison between SED and q-EELS, an ω scaling term must be applied (since atomic velocities relate to displacements via $u(t) = e^{-i \cdot (\omega \cdot t)}$ or $u(t, x) = e^{i \cdot (\omega \cdot t - k \cdot x)}$ and $v(t, x) = \frac{du(t, x)}{dt}$, therefore $v(t, x) = -i \cdot \omega \cdot u(t, x)$). Alternatively, displacements can be used in SED instead of velocities. When comparing to data, an additional ω scaling is often applied to the data, since the phonon population follows the Bose Einstein distribution (which can be roughly approximated as ω^{-1}). An additional

normalization could be introduced to account for atomic species by multiplying by the atomic form factor.

Lattice Dynamics

Phonon dispersions can be calculated via lattice dynamics (LD) (typically at zero temperature), which yields the eigenvectors (displacement associated with each atomic basis index) and frequencies of phonon modes in the harmonic approximation. Just as SED can be calculated on a monatomic basis to identify the waves occurring coherently over all atoms, LD calculations can be similarly “unfolded” by coherently summing the eigenvectors across each basis index. Each eigenvector is a 3D complex vector with a magnitude of unity, where the complex value denotes the phase of the mode. For certain optical modes where the atoms on alternating lattice sites are oscillating exactly out of phase, the eigenvectors sum to zero, and the waves interfere destructively. Examples of this will be shown in later sections. We use phonopy [14, 15] for LD calculations, with LAMMPS [9] used as a calculator for interatomic forces. The use of LAMMPS with phonopy allows for the same interatomic potential to be used for LD calculations and MD simulations.

While SED can be thought of as a measurement of the wavelike motion within the simulation, LD is computing the eigenmodes of vibration for the crystal. It is thus important to be precise when discussing the cancellation of modes when considering a different basis. Eigenvectors summing to zero does not imply the mode does not “exist” within the system for example. A mode, as defined by its frequency (ω), wavevector (k), and eigenvectors (ϵ), is a description of the wave and is linked to the basis on which the crystal is analyzed. An alternative description of coherent waves with all atoms participating (including coherence across each basis index) is not incompatible.

When comparing LD to q-EELS, one should keep in mind that LD typically calculates the available phonon modes (a density of states or a phonon dispersion) based on the harmonic solutions for given interatomic force constants. The actual population present in a finite-temperature system (or the *populated* density of states or dispersion) may differ. As discussed in the context of SED, the populated states follow the Bose-Einstein distribution, meaning a scaling by ω or ω^2 may be required for direct comparison between LD and q-EELS. Similarly, phonon softening or hardening has been observed in a variety of materials, whereby deviations may be expected between zero-temperature LD calculations and MD performed at a finite temperature.

Material System Selection

We begin with analysis of a simple model material, silicon, as it is well understood, simple to model, with fast and efficient atomic potentials. Silicon is also isotropic, which reduces the Brillouin zone directions required for analysis. For silicon, we use the Stillinger-Weber potential, with a lattice parameter of 5.43729 Å. For SED and our parallel-beam q-EELS simulations, our MD simulation volume consists of a $50 \times 50 \times 5$ conventional unit cell slab ($27.19 \times 27.19 \times 2.72$ nm) with periodic boundary conditions in all directions. As the primitive cell is half the size of the conventional cell, this yields 100 k points in each in-plane direction within the first Brillouin zone. We will evaluate vibrations occurring in the [001] plane (in the [100] direction: $\Gamma - \mathbf{X}$ and in [110]: $\Gamma - \mathbf{K}$). For our thickness-dependent series of convergent-beam simulations, we prepare a separate simulation of $400 \times 8 \times 8$ unit cells ($217.5 \times 4.35 \times 4.35$ nm). The 8 unit cell simulation width yields very poor reciprocal space resolution, but allows tracking of the q-EELS v-DOS signal through a large depth. For thickness-dependent q-EELS simulations, the exit wave is exported every 2.5 unit cells (13.6 nm). We run with timesteps of 2 fs, equilibrated under NVT for 1 ns, and under NVE for 2 ns. Following equilibration, positions and velocities are dumped every 20 fs, for an additional 10 ps (500 timesteps). This translates to a maximum measurable frequency of 25 THz ($f_{range} = 1/\Delta t$, where an FFT finds both positive and negative frequencies) and a frequency resolution of 0.1 THz ($\Delta\omega = 1/duration$).

We also consider AlN, using a DFT-trained deepMD potential. This potential has been validated previously and it faithfully reproduces the phonon dispersion (with the exception of near- Γ optical modes, where the local descriptor fails to capture long-range interactions). For AlN, we evaluate vibrations occurring in the [001] and [010] planes. In the [001] plane, the hexagonal structure is visible, which we use merely as a demonstration of the interferometric Brillouin zone. The [010] shows a different interferometric Brillouin zone, and also allows for comparison of anisotropic behavior between $\Gamma - \mathbf{K} - \mathbf{M}$ and $\Gamma - \mathbf{A}$ Brillouin zone directions (real-space and reciprocal-space structure shown in Figure 1). For the [001] plane simulations, we simulate a structure $50 \times 50 \times 2$ unit cells (using lattice constants $\mathbf{a} = 3.188930$ Å and $\mathbf{c} = 5.192357$ Å) using a skewed cell (non-orthogonalized). For simulations in the [010] plane, the system is $50 \times 2 \times 31$ unit cells (which translates to a roughly-square slab of 15.94×16.10 nm).

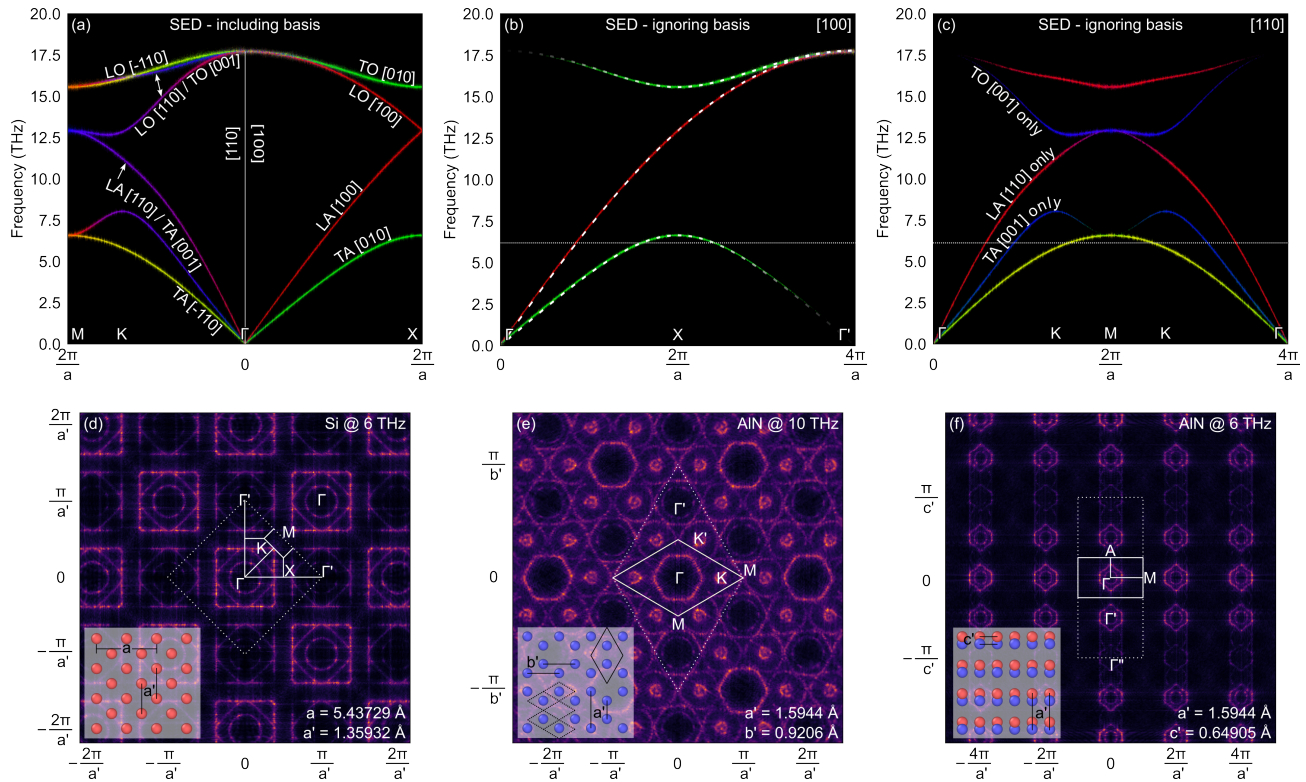


Figure 1. (a) SED calculations are performed for silicon on a diatomic basis (incoherent summing across the two atom primitive cell) in [100] (Γ - \mathbf{X}) and [110] (Γ - \mathbf{K} - \mathbf{M}) directions. Color is used to denote longitudinal modes (red), transverse in-plane modes (yellow), and transverse through-plane (z, blue). color mixing (i.e. blue+yellow=green, or red+blue=violet) indicates degenerate or mixed-polarization branches. When all atoms are summed coherently, an “unfolding” of the phonon branches occurs, shown for (b) the [100] (Γ - \mathbf{X}) and (c) [110] (Γ - \mathbf{K} - \mathbf{M}) directions. Coherent summing in LD (b, white dashed) shows the same effect. SED can also be performed over a range of angles to sweep the entire reciprocal space. These are shown at energy slices for (d) silicon in the [001] plane (showing the Γ - \mathbf{X} and Γ - \mathbf{K} - \mathbf{M} directions) (d) AlN in [001] (Γ - \mathbf{K} - \mathbf{M} and Γ - \mathbf{A}) and (e) AlN in [010] (Γ - \mathbf{K} - \mathbf{M} and Γ - \mathbf{A}). The real-space atomic configurations are shown inset, with conventional Brillouin zones shown in solid lines, and the interferometric Brillouin zones shown dotted.

RESULTS AND DISCUSSION

Observations of the interferometric Brillouin zone

We begin with an inspection of SED and LD for silicon performed with the traditional two-atom basis, and on the monatomic basis. This can be seen in Fig. 1.a-c. For analysis on the two-atom basis, SED produced the expected phonon dispersion in both [100] (Γ - \mathbf{X}) and [110] (Γ - \mathbf{K} - \mathbf{M}) directions (Fig. 1.a), and longitudinal (L) vs. transverse (T) modes are differentiated based on the direction of the velocity and position vectors used for the calculation of a given branch. In the monatomic case (coherent summing of reduced bases), the LO branch in [100] (Γ - \mathbf{X}) is only present in the second Brillouin zone (between $\frac{2\pi}{a}$ and $\frac{4\pi}{a}$) as these vibrations are equal in magnitude and 180° out of phase for each basis index. Within the first Brillouin zone, there is total destructive interference between the LO mode on each basis index. TA and TO branches fade in and fade out, as there is incomplete interference. In LD (Fig. 1.b, white dashed),

coherent summing of eigenvectors across each basis index gives the same fading effects due to partial or total destructive interference. In the [110] direction, branches appear to be missing (e.g. previously-degenerate LA and TA_z), however some branches may appear closer to Γ' (which is not sampled in a reciprocal path in the [110] direction). These missing branches will be observed in later sections. Note that we are not the first to observe missing branches and folding. For example, Li *et al.* [6] observed the systematic absence of phonon branches in q-EELS simulations, which they identify as resulting from the interference between waves on alternating bases. We would like to highlight that this is a fundamental behavior of phonons however, as this is observable even without the electron scattering effects included.

We can see that Γ points in SED (and likewise, the Dynamic Structure Factor) are non-equivalent; $\Gamma_0 \neq \Gamma_1$ and so on, and there is a new minimum repeating unit in reciprocal space. Performing SED across a sweep of angles so as to map the entire reciprocal space across the [001] plane (Fig. 1.d, plotting an intensity map at a fixed

energy slice), the presence of this new minimum repeating unit becomes increasingly apparent. For clarity, we introduce the terminology “gamma prime” (Γ') to refer to the non-equivalent gamma points in reciprocal space, and we refer to the new minimum repeating area as an “interferometric Brillouin zone”, where the center of this new interferometric Brillouin zone is Γ , and may contain (or extend to) one or more Γ' points. Γ' correspond to the forbidden Bragg diffraction points, while Γ corresponds to the allowed points. The concept of the static structure factor and the interferometric Brillouin zone (tied to the Dynamic Structure Factor) are thus closely related, however we believe the interferometric Brillouin zone concept is useful for understanding the phonon behavior within many systems.

To understand the interferometric Brillouin zone further and show that this is not unique to silicon, we show AlN in the [001] plane (Fig. 1.e, containing Γ - \mathbf{K} - \mathbf{M} and Γ - \mathbf{M}) and the [010] plane (Fig. 1.f, containing Γ - \mathbf{K} - \mathbf{M} and Γ - \mathbf{A}). The real-space atomic configurations for each plane are shown inset for each case. We find that the size of the interferometric Brillouin zone is defined by the minimum interatomic spacing in a given direction (where we introduce the \mathbf{a}' vs. \mathbf{a} notation and so on, where \mathbf{a}' denotes the interatomic spacing and \mathbf{a} denotes the unit cell). This can be understood as vibrational waves existing across the system, where the minimum interatomic spacing (rather than the primitive cell size) defines the minimum sampling of these waves. In the case of AlN [001] (Fig. 1.e), the interferometric Brillouin zone contains a Γ' points in the Γ - \mathbf{M} direction, but is the same size in the Γ - \mathbf{K} - \mathbf{M} direction. Drawing this interferometric Brillouin zone in real space, we find that it corresponds to a rhombus drawn around a single atom. While this rhombus is much smaller than the primitive cell, this would be the primitive cell if all atoms were equal and atoms were inserted in the center of each hexagon. Thinking in terms of vacancies and the virtual crystal approximation [16–18] (where vacancy sites or substitutional atoms are not considered to break the crystallinity), the monoatomic sampling is not sensitive to missing atoms, but *is* sensitive to sampling on a periodicity smaller than the primitive unit cell. Similarly with silicon, the interferometric Brillouin zone’s real-space volume corresponds to a cube drawn around a single atom. The missing atom on alternating tetrahedral sites does not affect the sampling of the wave (and filling in the missing atoms reduces the structure to simple cubic). For AlN in the [010] plane (Fig. 1.f), we again see an interferometric Brillouin zone extending multiple Brillouin zones, this time past Γ' and to Γ'' . This again corresponds to the minimum atomic spacing in real space.

Understanding selection rules

We begin with q-EELS simulations using a parallel beam, as the diffraction disks resulting from a convergent STEM probe contribute to the linewidths of any acquired phonon dispersions. The electron energy is 100 keV, propagated through the face of the MD-simulated slab, using a 0.5 Å lateral sampling and 1 Å slice thickness. The result is a data cube in $\omega, \mathbf{k}_x, \mathbf{k}_y$, which can be sliced along an arbitrary reciprocal vector to produce a phonon dispersion. We show one such slice path in Figure 2.a below, tracing in two [110] directions and then in [100]. This reciprocal path is chosen so as to acquire all branches in [110], as some branches are only visible around Γ or Γ' . Similarly, selection rules prohibit the observation of some branches in specific interferometric Brillouin zones (as will be discussed below). The data cube can also be sliced at a given ω to produce an energy-resolved diffraction pattern. Several of these can be seen in Figure 2.b-e, and additional slices are shown in the Supplemental Material.

At low-frequencies, rings or crescents can be observed in the energy-resolved diffraction images, centered about each Γ point, with a radius according to the phonon modes’ wavevector \mathbf{k} (Fig. 2.b,c). The unfolding of the phonon branches into the interferometric Brillouin zone again applies, shown in Fig. 2.a, with color-coded arrows identifying the [100] longitudinal modes in each energy slice (Fig. 2.b-e). As the frequency is increased, crescents associated with longitudinal modes continue to move away from the Γ points, crossing the conventional Brillouin zone boundary (Fig. 2.d, according to monatomically sampled phonon dispersion), and eventually converging on Γ' , or the interferometric Brillouin zone corners (Fig. 2.e).

Nicholls *et al.* [3] highlighted the presence of a $\mathbf{q} \cdot \boldsymbol{\varepsilon}$ term in the scattering cross-section, where \mathbf{q} is the vector of momentum transferred to the fast electron and $\boldsymbol{\varepsilon}$ is the phonon eigenvector (i.e., the direction of vibrational displacements). In simple terms, the electron only gains momentum in a given direction due to atomic displacements (or the component of atomic displacements) in that same direction. The result is polarization selectivity in the q-EELS signal, leading to the observation of crescents as opposed to fully-enclosed circles. Within the first interferometric Brillouin zone, $\mathbf{q} \cdot \boldsymbol{\varepsilon}$ is only nonzero for modes where displacements are parallel to \mathbf{q} , i.e., the first interferometric Brillouin zone has 100% selectivity for longitudinal modes. For outer interferometric Brillouin zones, we see crescents which fade to zero intensity where atomic displacements ($\boldsymbol{\varepsilon}$) of longitudinal or transverse modes become perpendicular to \mathbf{q} . The same branches can also be seen in different interferometric Brillouin zones, with crescents in different directions. An example is shown in Fig. 2.b, where the lower interfer-

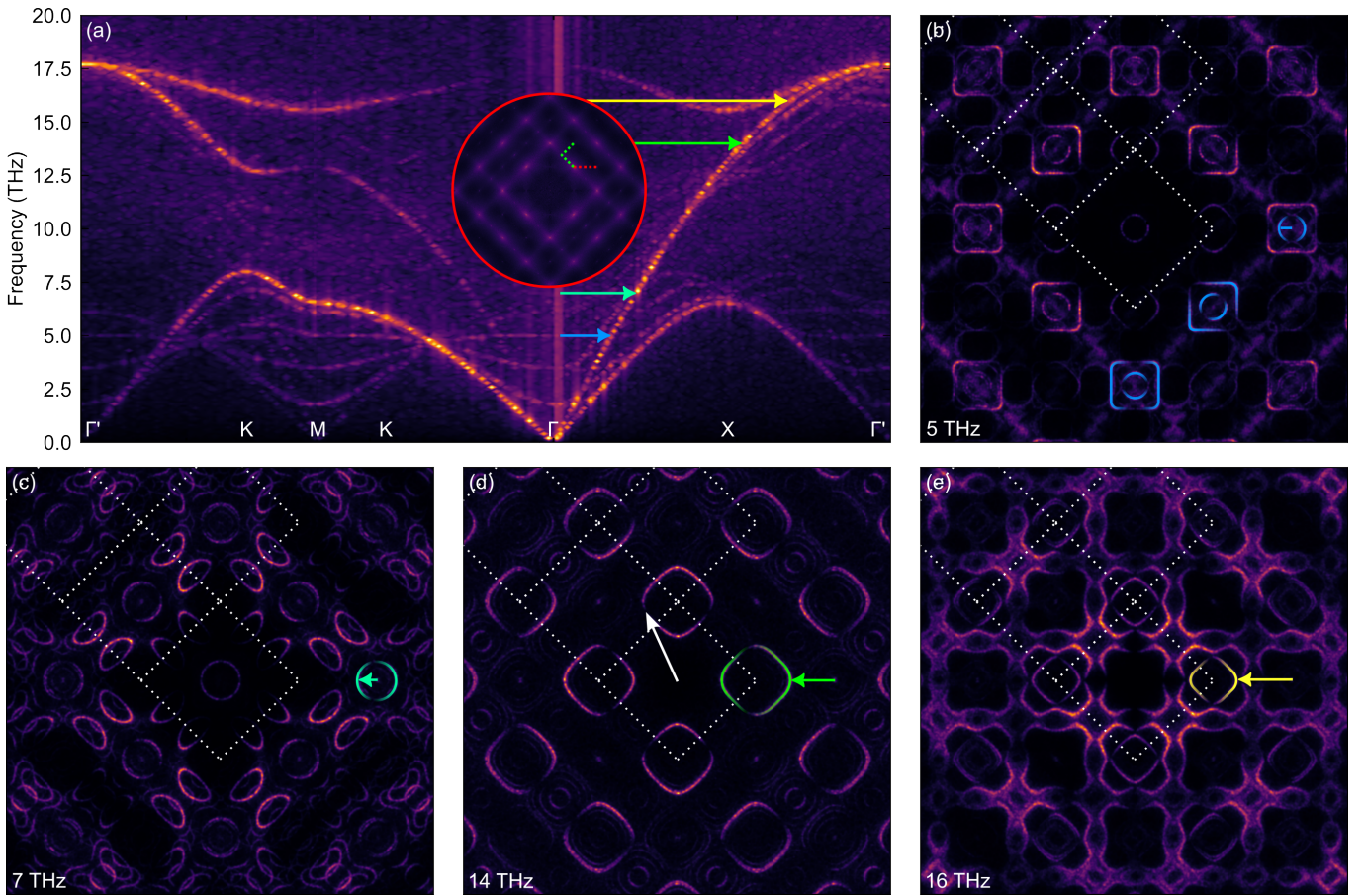


Figure 2. (a) phonon dispersions can be generated from q-EELS assuming the appropriate reciprocal paths can be selected. The sampled path is shown inset, with a path to Γ' required to capture [110] TO branches. Faint spurious branches can also be observed, particularly crossing Γ at finite ω , however these will be discussed in a subsequent section. Selected energies are highlighted in blue/cyan/green/yellow corresponding to the energy-resolved diffraction images at 5 THz (b), 7 THz (c), 14 THz (d) and 16 THz (e). The interferometric Brillouin zone is shown in dotted white, and crescents corresponding to the longitudinal [100] branch can be seen to continue increasing in distance from each Γ point even as we cross the traditional (folded) Brillouin zone boundary. The orientation of the crescents can be used to determine the phonon branch polarization according to $\mathbf{q} \cdot \boldsymbol{\varepsilon}$, where \mathbf{q} is the vector from the center (total momentum exchange) and $\boldsymbol{\varepsilon}$ is the phonon eigenvector (or the direction of atomic displacements). This yields a total selectivity for longitudinal modes within the first Brillouin zone.

ometric Brillouin zone contains up-pointing and down-pointing crescents at small \mathbf{k} corresponding to longitudinal modes. These same modes in the right interferometric Brillouin zone point to the left and right, most intense where $\mathbf{q} \cdot \boldsymbol{\varepsilon}$ is unity. In the lower interferometric Brillouin zone, the outer rounded-squares correspond to transverse modes at higher \mathbf{k} with the eigenvector along \mathbf{q} . These features can again be seen rotated in the lower-right and right-most interferometric Brillouin zones.

It may be intuitive to take advantage of these selection rules by acquiring a vibrational spectrum from an outer Brillouin zone to obtain a polarization-selective density of states (i.e., a density of states associated with vibrations in only one direction). The lateral component of vector \mathbf{q} should not be ignored, however. Within Fig. 2.d for example, the longitudinal crescents further from the center are longer, and the point of minimum intensity is

directly in line with \mathbf{q} (identified with a white arrow). In other words, the vector to each point in reciprocal space determines the direction the electron is sensitive to (*not* the vector to the center of the interferometric Brillouin zone). This means summing over any given area in reciprocal space (as a result of finite collection geometries or instrumental momentum uncertainty) will have some off-angle eigenvector components and outer interferometric Brillouin zones do not have 100% selectivity for a given polarization.

Thus far, we have not discussed through-plane vibrations. In the [110] direction, only TA [001] and TO [001] branches (i.e., transverse branches with displacements in the through-plane direction) appear between Γ and Γ' (while the degenerate LA/LO branches appear closer to Γ'). These TA [001] / TO [001] branches are clearly visible in SED in Fig. 1.c, but they are noticeably absent

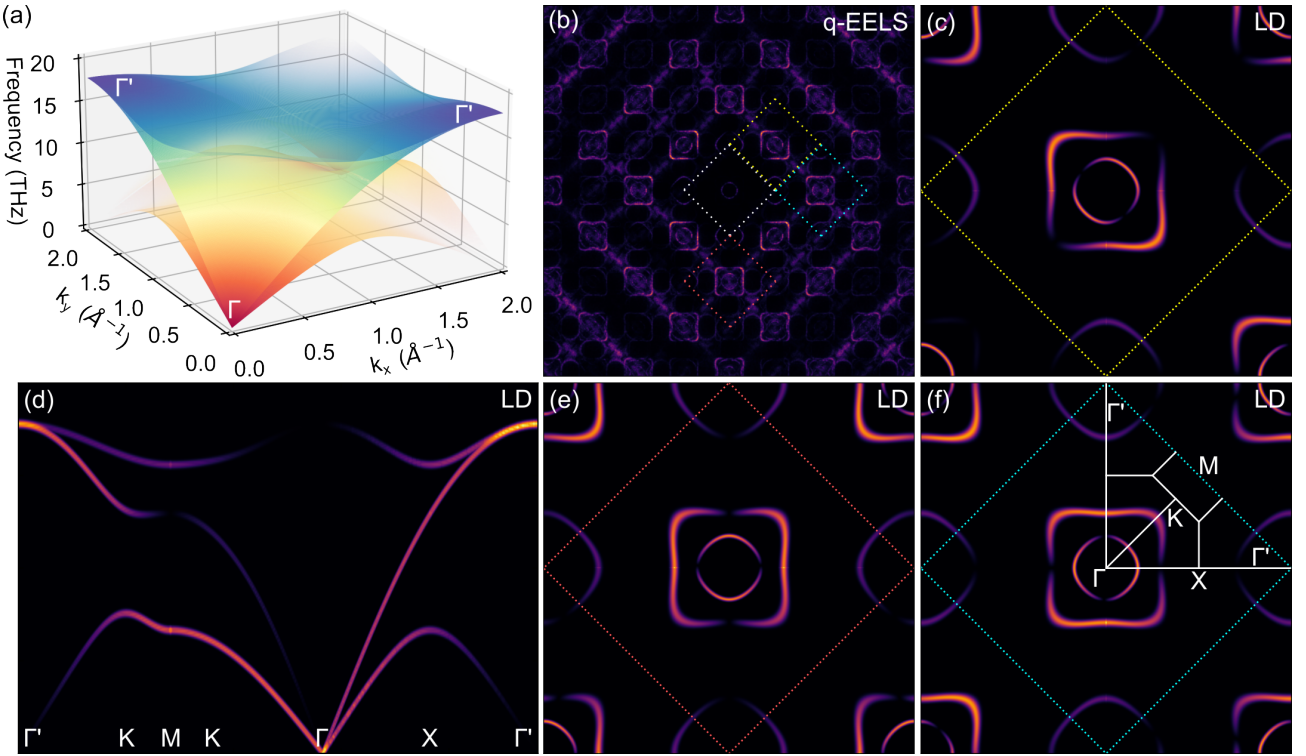


Figure 3. (a) Lattice Dynamics (LD) across a grid of reciprocal points and coherent summing of eigenvectors allows for reconstruction of the unfolded phonon surface and interferometric Brillouin zone observed by q-EELS. (b) the 5 THz energy slice from q-EELS is shown, with interferometric Brillouin zones shown in dotted in white. These energy slices can be approximately replicated by incorporating selection rules into LD (c,e,f), shown for the upper-right, lower, and right-most interferometric Brillouin zones respectively. Taking slices in reciprocal space (same path as in Figure 2), dispersions can also be replicated (d).

between $\Gamma-K-M$ in q-EELS (in Fig. 2.a, or between Γ points at 14 THz in Fig. 2.d). The Ewald sphere suggests the through-plane component of vector \mathbf{q} will increase as the length of \mathbf{q} increases, meaning we should have increased sensitivity to through-plane vibrations at high \mathbf{q} . Examining Fig. 2.d closely, we indeed see the presence of small rings between Γ points at high \mathbf{q} , which is evidence of this growing through-plane sensitivity (TO [001] branches).

Using LD and SED as a first-approximation for q-EELS

The primary features in the energy slices shown above include the unfolding of portions of the phonon dispersions (due to coherent sampling of the waves on a monatomic basis), and selection for the eigenvector component along \mathbf{q} . This behavior can also be replicated by extracting energy slices from LD or SED. Using phonopy [14, 15], we calculate the eigenvectors across a grid of \mathbf{q} points extending out to six conventional Brillouin zones. Summing eigenvectors across atomic bases yields the unfolded dispersion surfaces (shown in Fig. 3.a).

By filtering eigenvectors by direction (taking the com-

ponent in the direction pointing away from the central Γ) and applying a thickness to each surface, we find we are able to reasonably reproduce the simulated q-EELS signal with selection rules included. A dispersion is shown in Fig. 3.d for the same reciprocal path used in Fig. 2.a, and the same branches and fading effects can be seen (e.g. $\Gamma-X-\Gamma'$ T[100]). Taking slices in energy, we also show replication of the energy-resolved diffraction images from q-EELS (5 THz slices shown in Fig. 3.b for q-EELS and Fig. 3.c,e,f generated from LD). These simulations are extremely computationally cheap by comparison to q-EELS, and maybe a viable approach for those primarily interested in predicting kinematic scattering from single-phonon contributions only.

Selection rules for a convergent beam

In the previous section, we saw the presence of selection rules under parallel-beam illumination, where certain phonon polarizations are only observable in certain Brillouin zones or areas of Brillouin zones. It may thus be intuitive to attempt a dark-field EELS measurement with a convergent probe in an effort to obtain a localized polarization-selective vibrational density of states

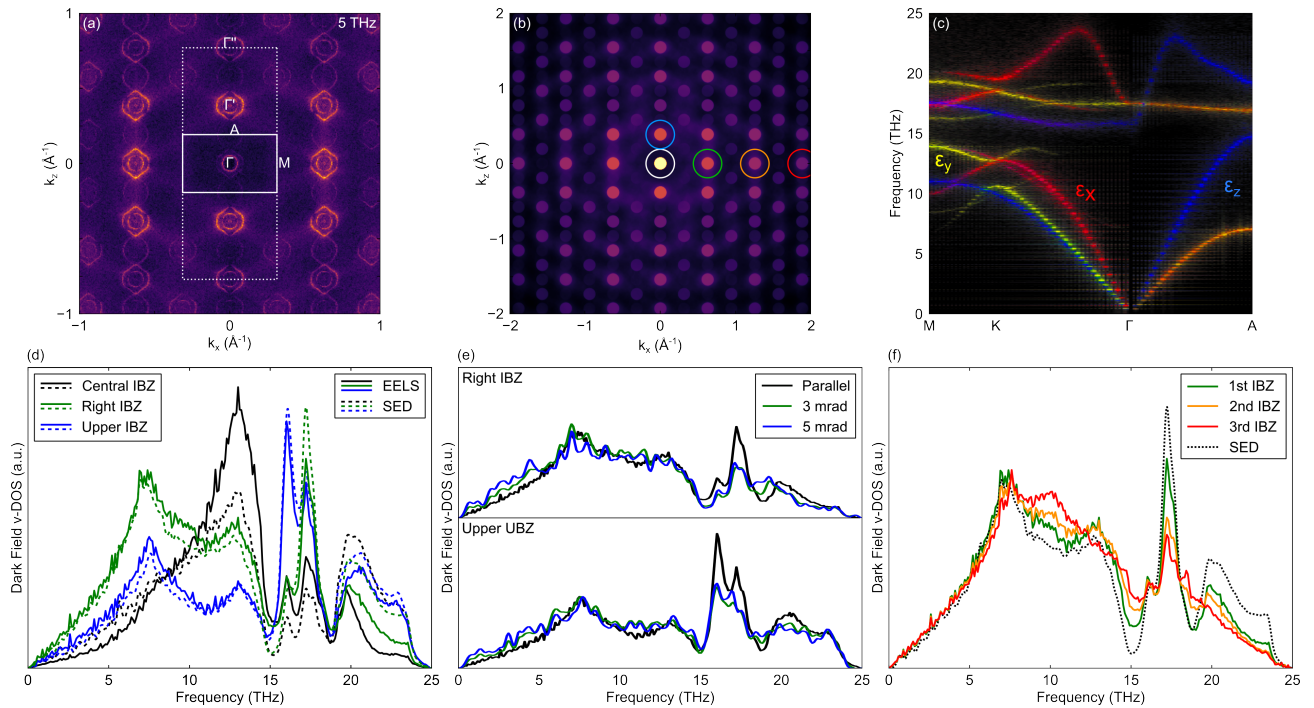


Figure 4. (a) energy-resolved diffraction images from the parallel-beam case are used to inform selection of brillouin zones and mask diameter. (b) For the 3 mrad convergence angle case, circular masks are applied (with radius $1/c$), centered on several Γ points. (c) The phonon dispersions are shown for the $\Gamma-K-M$ and $\Gamma-A$ directions from SED, however all angles in reciprocal space are used to calculate v-DOS from SED. red/yellow/blue denotes polarization in x (along $\Gamma-K-M$), y (through-plane), and z (along $\Gamma-A$). (d) We compare the central, right, and upper Brillouin zones (black, green, and blue, respectively) between q-EELS (solid) and calculations from SED (dashed) using displacements along \mathbf{q} , or x and z . (e) Slightly reduced selectivity is seen as the convergence angle is increased between parallel illumination (solid), 3 mrad (dashed) or 5 mrad (dotted). (f) increased selectivity should be obtained at outer Brillouin zones, however multiple scattering and sensitivity to through-plane displacements may obscure this effect.

(v-DOS). To explore this possibility, we move to our second material system: AlN viewed in the [010] direction, which has a moderately anisotropic v-DOS between $\Gamma-K-M$ and $\Gamma-A$ directions. Under parallel beam illumination, the energy-resolved diffraction images appear as expected (example shown in Fig. 4.a). We first run the q-EELS simulations using a 3 mrad convergence angle (chosen based on the size of the Bragg disks, to avoid overlapping of disks and sampling of multiple Brillouin zones). We then apply a $1/c$ radius mask in reciprocal space, centered on various Γ points, and perform an incoherent sum within the mask to acquire a dark-field EELS v-DOS signal.

To acquire a comparable signal from SED, the dispersions are calculated out to multiple reciprocal units and across a range of angles, and a similar masking operation is performed. Merely summing the dispersions acquired in the high-symmetry directions (or taking the FFT of velocities from MD in each direction) is insufficient, as it does not account for all modes across reciprocal space and may capture modes at reciprocal points outside of the dark field aperture (mask). The velocity components used for SED depend on the dark-field EELS spectrum

of interest. If velocities along the \mathbf{q} direction are used, this will be directly comparable to the $\mathbf{q} \cdot \boldsymbol{\varepsilon}$ selectivity in q-EELS. Alternatively, any of the three Cartesian directions can be used to obtain a polarization-specific “ground truth” spectrum for eigenvectors within the selected reciprocal area.

Starting by comparing the central, right, and upper Brillouin zones, these should have selectivity for longitudinal modes, and vibrations in x and z respectively. These are shown in Figure 4.d (black, green, and blue, respectively), and reasonable agreement is seen between the spectrum acquired from q-EELS and SED (solid and dashed, respectively). In theory this selectivity should be reduced as an increased convergence angle is used, as the diffraction disks now cover a larger reciprocal area and greater summing over reciprocal space is captured. This is shown in Figure 4.e for the parallel beam case, and a 3 mrad and 5 mrad convergence angle (solid, dashed, and dotted, respectively).

Finally, it may be intuitive that higher-order Brillouin zones should yield a better selectivity for a given polarization. To check for this possibility, we examine three Brillouin zones in the $\Gamma-K-M$ direction (ignoring the $\Gamma-A$

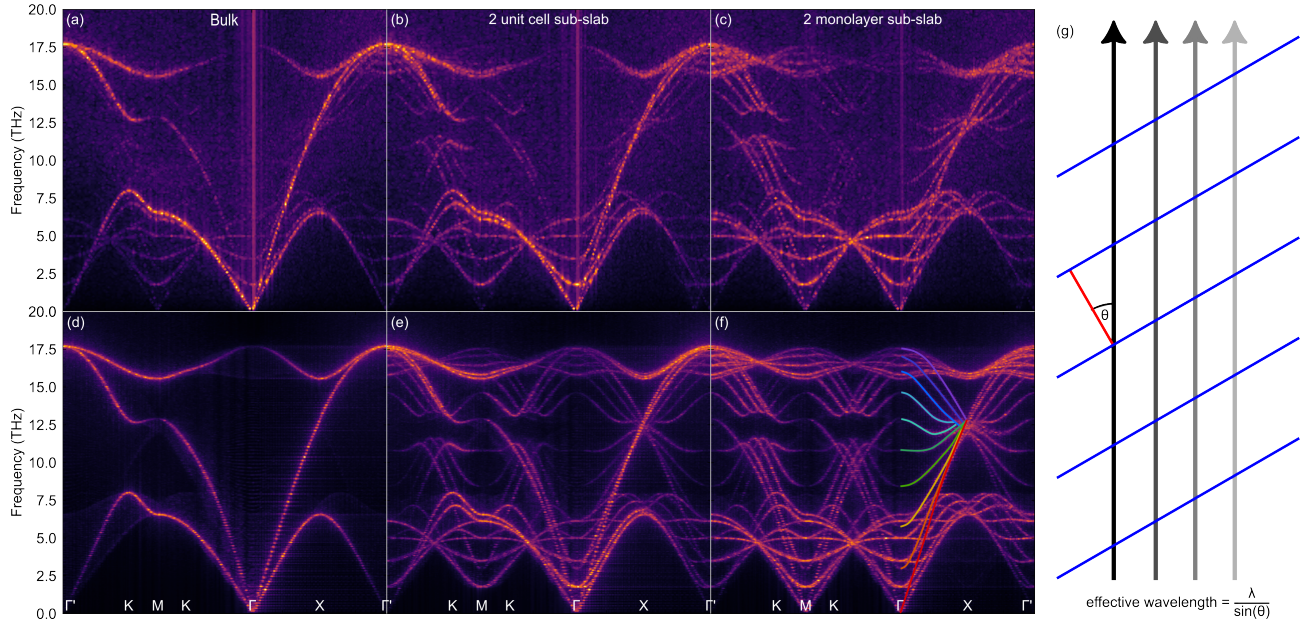


Figure 5. Dispersions are generated along the same reciprocal path for q-EELS (a-c) and SED (d-f) for the bulk (a,d), a slab trimmed to 2 unit cells (b,e), and a slab trimmed to 2 monolayers (c,f). Spurious branches are visible in the bulk q-EELS case, which we attribute to an antenna-like effect, where the projection of through-plane modes can be detected if layers are not sampled uniformly (f). Destructive interference prevents their observation in bulk SED, however non-uniform sampling in EELS as a function of depth means they can be observed. In our system, there are 10 discrete out-of-plane branches (highlighted in f), corresponding to the 10 primitive cells in the through-plane direction.

direction due to the large interferometric Brillouin zone in \mathbf{z}). These results are shown in Figure 4.f compared against the v-DOS spectrum from SED. We actually see a worsening selectivity, likely due to increasing sensitivity to through-plane vibrations and multiple scattering effects (where SED only matches the single-phonon term in the dynamic structure factor).

Phantom branches within q-EELS phonon dispersions

Spurious branches appear in the simulated q-EELS dispersions in Fig.2.a, particularly visible near Γ . To understand their source, we examine the thickness-dependent results from our q-EELS simulations. We found these phantom branches were brighter for the wave shallower within the simulation, suggesting that these branches are inherent to the system, but that a destructive interference effect is hiding them in the thicker simulations. We also perform SED across the same structure, by trimming the system to the first several atomic monolayers, and we observe these phantom branches here as well. Dispersion from identical reciprocal paths are shown in Figure 5 for q-EELS (a,b,c) and SED (d,e,f), for bulk, a 2 unit cell (8 monolayer), and 2 monolayer trimmed system.

We attribute these phantom branches to an antenna-like effect: for a wave traveling orthogonal to the sam-

pled direction, the wave may be picked up with an apparent wavelength corresponding to the sine of the angle between wave and sampling direction (i.e., the projection of the wave onto the sampling direction). Such a feature is not observed in SED when the entire system is sampled uniformly however, as all phases of this orthogonal wave are sampled and interfere destructively. A schematic for this phenomena is shown in Figure 5.g, where non-uniform sampling (black/gray arrows) of the wavefront (blue) means that full phase cancellation does not occur, and the projected wavelength is observed.

Within q-EELS, the upper layers of the sample are disproportionately sampled (as will be demonstrated in the following section). Discrete branches are seen due to a discrete number of through-plane modes, and in the thinnest case, ten branches can be counted (highlighted in 5.f) corresponding to our MD simulation's ten primitive-cell slab thickness (20 monolayers). Additional discussion on the origin of these branches is included in the Supplemental Material. We used periodic boundary conditions in these simulations, meaning through-plane modes should be expected (waves exiting the top of the slab and re-entering through the bottom), however a subsequent MD simulation with a thin slab in vacuum (shown in the Supplemental Material) yielded similar results. For a finite-thickness suspended film, through-plane waves may exist, reflecting off the top and bottom surface. Assuming sufficient measurement sensitivity can

be acquired, we predict that these through-plane modes should be observable in experiment.

Thickness effects

To evaluate the presence of thickness effects in q-EELS simulations, we prepared an additional MD simulation of $400 \times 8 \times 8$ unit cells of silicon, with the multislice simulation propagating the electron wave along the 400 unit cell direction. Convergent STEM probes (30 mrad, 5 mrad, and 3 mrad) are propagated, and the exit wave is recorded as a function of depth. Summing the entire v-DOS spectrum yields a signal intensity as a function of depth, which we have presented in Figure 6.a. To better visualize the depth-distribution of the acquired signal, the derivative of the spectrum intensity is taken (Figure 6.b) to obtain the signal attributed to each slice. Regardless of convergence angle, shallower regions of the sample have a higher contribution to the signal (steeper in Figure 6.a, higher signal per layer in Figure 6.b). This depth-varying contribution to the signal is what yields the sensitivity to the through-plane branches in q-EELS seen in Fig 5. We also see the Pendellösung effect (periodic oscillations in signal intensity) which comes from dynamic scattering effects.

A series of simulations were also run with a finer depth-resolution (0.25 unit cell), shown in the inset of Figure 6.a. Interestingly, a stepped behavior in the 30 mrad case is seen. In the diamond cubic structure in [001], an atomic column has an atom on every other monolayer. If atomic resolution is obtained (as in the 30 mrad case), this feature results in near-zero additional signal for the monolayers without atoms. For the 3 and 5 mrad cases, the loss of atomic resolution yields a blurring of this effect.

CONCLUSION

In this work we have shown the presence of a so-called “interferometric Brillouin zone”, which is a larger minimum repeating unit in reciprocal space, defined by the interatomic spacing rather than the size of the primitive cell. This phenomena arises from interference of phonons on each atomic basis index, and yields a vibrational non-equivalency between traditional Brillouin zones. The interferometric Brillouin zone has been observed in fast-electron experiments [6], and the behavior is observed here without considering the incident electron’s interaction.

We also investigated the effects of selection rules [3], where the fast-electron momentum exchange is directly tied to the direction of atomic displacements (eigenvectors). The result is the disappearance of specific phonon branches within certain Brillouin zones, which can be

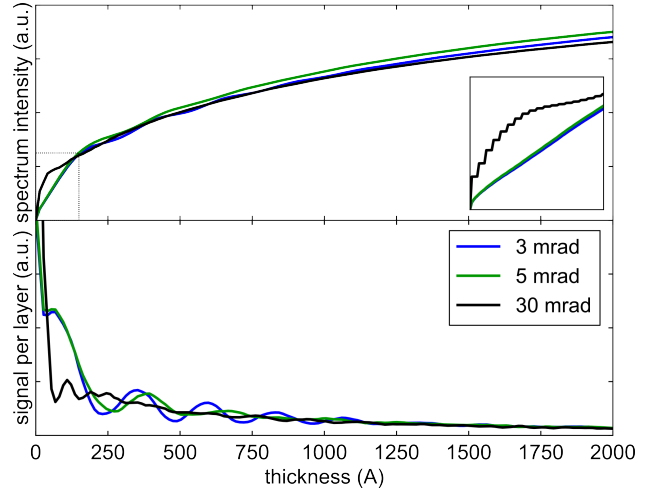


Figure 6. (a) The q-EELS signal intensity is simulated over the depth of a 400 unit cells of silicon (217 nm) by summing over the v-DOS from the multislice exit wave at multiple points. In the inset, a finer spatial resolution is used and the stepped behavior is seen for the 30 mrad implying atomic resolution is obtained. (b) The signal acquired on a per-layer basis can be found by taking the derivative of the total signal as a function of depth. In both cases, the highest signal comes from the upper layers of the sample. Dynamic effects (Pendellösung oscillations) can also be seen.

used to acquire a polarization-selective vibrational density of states (v-DOS) measurement.

Based on our understanding of selection rules, and noting the equivalence of Spectral Energy Density (SED) with the single-phonon scattering terms in the dynamic structure factor, we also introduce a simulation method using SED and Lattice Dynamics (LD), able to reproduce the q-EELS signal to a first approximation.

Finally, we note the presence of spurious branches in the q-EELS phonon dispersions, which we attribute to a varying sensitivity with depth. When the full system is non-uniformly sampled (e.g., disproportionately high sampling of the upper surface), sensitivity to through-plane modes can be obtained (a phenomena which is distinct from the through-plane component of the Ewald sphere). This has not been observed in experiment, but we predict that with sufficient signal and momentum/energy resolution, this phenomena could be observed.

ACKNOWLEDGEMENTS

ACKNOWLEDGMENTS

Research was supported as part of APEX (A Center for Power Electronics Materials and Manufacturing Exploration), an Energy Frontier Research Center funded by the U.S. Department of Energy (DOE), Office of Science,

Basic Energy Sciences (BES), under Award #ERW0345 (computational studies and analysis).

This work was also supported by the Center for Nanophase Materials Sciences (CNMS), a U.S. Department of Energy, Office of Science User Facility and the U.S. Department of Energy, Office of Basic Energy Sciences (DOE-BES), Division of Materials Sciences and Engineering under contract ERKCS89.

Work at Vanderbilt was supported by the U.S. Department of Energy, Office of Science User Facility and the U.S. Department of Energy, Office of Basic Energy Sciences (DOE-BES), Division of Materials Sciences and Engineering grant DE-FG02-o0ER464 and by the McMinn Endowment.

This work was led equally by University of Virginia and Oak Ridge National Laboratory.

* twp4fg@virginia.edu

† hoglunder@ornl.gov

‡ peh4v@virginia.edu

- [1] Paul M. Zeiger and Ján Rusz. Frequency-resolved frozen phonon multislice method and its application to vibrational electron energy loss spectroscopy using parallel illumination. *Phys. Rev. B*, 104:104301, Sep 2021.
- [2] José Ángel Castellanos-Reyes, Paul M. Zeiger, and Ján Rusz. Dynamical theory of angle-resolved electron energy loss and gain spectroscopies of phonons and magnons in transmission electron microscopy including multiple scattering effects. *Phys. Rev. Lett.*, 134:036402, Jan 2025.
- [3] R. J. Nicholls, F. S. Hage, D. G. McCulloch, Q. M. Ramaesse, K. Refson, and J. R. Yates. Theory of momentum-resolved phonon spectroscopy in the electron microscope. *Phys. Rev. B*, 99:094105, Mar 2019.
- [4] Eric R. Hoglund, Harrison A. Walker, Kamal Hussain, De-Liang Bao, Haoyang Ni, Abdullah Mamun, Jefferey Baxter, Joshua D. Caldwell, Asif Khan, Sokrates T. Pantelides, Patrick E. Hopkins, and Jordan A. Hachtel. Nonequivalent atomic vibrations at interfaces in a polar superlattice. *Advanced Materials*, 36(33):2402925, 2024.
- [5] Hongbin Yang, Yinong Zhou, Guangyao Miao, Ján Rusz, Xingxu Yan, Francisco Guzman, Xiaofeng Xu, Xianghan Xu, Toshihiro Aoki, Paul Zeiger, Xuetao Zhu, Weihua Wang, Jiandong Guo, Ruqian Wu, and Xiaoqing Pan. Phonon modes and electron-phonon coupling at the fese/srtio3 interface. *Nature*, 635(8038):332–336, Nov 2024.

- [6] Aowen Li, Paul M. Zeiger, Zuxian He, Mingquan Xu, Stephen J. Pennycook, Ján Rusz, and Wu Zhou. Systematic Absences of Optical Phonon Modes in Phonon Dispersion Measured by Electron Microscopy. *Physical Review Letters*, 133(4):46101, 2024.
- [7] John A Thomas, Joseph E Turney, Ryan M Iutzi, Cristina H Amon, and Alan J H McGaughey. Predicting phonon dispersion relations and lifetimes from the spectral energy density. *Physical Review B - Condensed Matter and Materials Physics*, 81(8):1–4, 2010.
- [8] B. D. Forbes, A. V. Martin, S. D. Findlay, A. J. D’Alfonso, and L. J. Allen. Quantum mechanical model for phonon excitation in electron diffraction and imaging using a born-oppenheimer approximation. *Phys. Rev. B*, 82:104103, Sep 2010.
- [9] A. P. Thompson, H. M. Aktulga, R. Berger, D. S. Bolintineanu, W. M. Brown, P. S. Crozier, P. J. in ’t Veld, A. Kohlmeyer, S. G. Moore, T. D. Nguyen, R. Shan, M. J. Stevens, J. Tranchida, C. Trott, and S. J. Plimpton. LAMMPS - a flexible simulation tool for particle-based materials modeling at the atomic, meso, and continuum scales. *Comp. Phys. Comm.*, 271:108171, 2022.
- [10] Jacob Madsen and Toma Susi. abTEM: Transmission electron microscopy from first principles. *Open Research Europe*, 1(24):13015, 2021.
- [11] K. Sturm. Dynamic structure factor: An introduction. *Zeitschrift für Naturforschung A*, 48(1-2):233–242, 1993.
- [12] Neil W. Ashcroft and N. David Mermin. *Solid State Physics*. Brooks Cole, 1 edition, January 1976.
- [13] Léon Van Hove. Correlations in space and time and born approximation scattering in systems of interacting particles. *Phys. Rev.*, 95:249–262, Jul 1954.
- [14] Atsushi Togo, Laurent Chaput, Terumasa Tadano, and Isao Tanaka. Implementation strategies in phonopy and phono3py. *J. Phys. Condens. Matter*, 35(35):353001, 2023.
- [15] Atsushi Togo. First-principles phonon calculations with phonopy and phono3py. *J. Phys. Soc. Jpn.*, 92(1):012001, 2023.
- [16] B. Abeles. Lattice thermal conductivity of disordered semiconductor alloys at high temperatures. *Phys. Rev.*, 131:1906–1911, Sep 1963.
- [17] L. Bellaiche and David Vanderbilt. Virtual crystal approximation revisited: Application to dielectric and piezoelectric properties of perovskites. *Phys. Rev. B*, 61:7877–7882, Mar 2000.
- [18] Thomas Beechem, Samuel Graham, Patrick Hopkins, and Pamela Norris. Role of interface disorder on thermal boundary conductance using a virtual crystal approach. *Applied Physics Letters*, 90(5):054104, 01 2007.

1 **Understanding phonon selection and interference in**
2 **momentum-resolved electron energy loss spectroscopy -**
3 **Supplemental Material**

4 Thomas W. Pfeifer^{*}

5 *Department of Mechanical and Aerospace Engineering,*
6 *University of Virginia, Charlottesville, Virginia 22920, USA*

7 Harrison A. Walker and Sokrates Pantelides

8 *Department of Interdisciplinary Materials Science,*
9 *Vanderbilt University, Nashville, Tennessee 37235, USA*

10 Henry Aller and Samuel Graham

11 *Department of Mechanical Engineering,*
12 *University of Maryland, College Park, Maryland 20742, USA*

13 Jordan A. Hachtel and Eric R. Hoglund[†]

14 *Center for Nanophase Materials Sciences,*
15 *Oak Ridge National Laboratory, Oak Ridge, Tennessee 37830, USA*

16 Patrick E. Hopkins[‡]

17 *Department of Mechanical and Aerospace Engineering,*
18 *University of Virginia, Charlottesville, Virginia 22920, USA*

19 *Department of Physics, University of Virginia,*
20 *Charlottesville, Virginia 22920, USA and*

21 *Department of Materials Science and Engineering,*
22 *University of Virginia, Charlottesville, Virginia 22920, USA*

²⁴ **I. SUPPLEMENTAL MATERIAL**

²⁵ **A. Code availability**

²⁶ Our q-EELS simulations tools are available at <https://github.com/tpchuckles/abEELS>.

²⁷ This tool accepts an input configuration file (samples available on github as well) which
²⁸ specifies the LAMMPS output files, atom types, system size and timestep information.

²⁹ Optional system trimming/tiling/rotation parameters are included as well. Both FRFPMS
³⁰ and TACAW can be run. Generation of frequency bins (for FRFPMS) is performed, and
³¹ the multislice calculation is done via abtem. Post-processing tools are included: v-DOS,
³² phonon dispersions via traces along reciprocal paths, or energy-resolved diffraction images.

³³ Our SED code is available at <https://github.com/tpchuckles/pySED>. Common functions
³⁴ are available, which can be imported into any python script. Example scripts are also
³⁵ included in the “examples” folder, showing generation of dispersions in various materials
³⁶ and reciprocal directions.

³⁷ **B. A mathematical comparison between Spectral Energy Density and the Dy-
³⁸ namic Structure Factor**

³⁹ In the works of Thomas *et al.*, SED is presented as:

$$\Phi(\omega, k) = \frac{1}{4\pi\omega_f N_T} \sum_{\alpha} \sum_j^B \left| \int_0^{\omega_f} \sum_n^N v_{\alpha,n,j}(t) \cdot \exp[i \cdot k \cdot \bar{r}_{\beta,n,j=0} - i \cdot \omega \cdot t] dt \right|^2 \quad (S1)$$

⁴⁰ where the atom is referenced by its unit cell (n) and basis index within the unit cell
⁴¹ (j), with its velocity at a given timestep ($v_{\alpha,n,j}(t)$) and average position ($\bar{r}_{\beta,n,b=0}$) used to
⁴² calculate its contribution to the phonon. All atoms for a given basis are coherently summed,
⁴³ and bases are incoherently summed. In our simplified expression:

^{*} twp4fg@virginia.edu

[†] hoglunder@ornl.gov

[‡] peh4v@virginia.edu

$$\Phi(\omega, k) = \sum_{\alpha} \left| \int_0^{\omega_f} \sum_n v_{\alpha, n}(t) \cdot e^{i \cdot k \cdot \bar{r}_{\beta, n} - i \cdot \omega \cdot t} dt \right|^2 \quad (S2)$$

44 we ignore the atomic basis, and instead consider the coherent wavelike motion of all
 45 atoms.

46 Expressions for the dynamic structure factor can be found in many forms in the literature,
 47 however for our purposes, we use the expression from Ashcroft & Mermin [1], specifically
 48 their equation N.18:

$$S(q, \omega) = e^{-2W} \int \frac{1}{2\pi} e^{i\omega t} \sum_R e^{-iqR} e^{\langle [q \cdot u(0)][q \cdot u(R, t)] \rangle} dt \quad (S3)$$

49 This is states to be the exact solution for a harmonic crystal, where R is the vector used
 50 to identify an atom, u us the displacement of the atom at R and time t , and W is related
 51 to the Debye Waller factor. Following along with Ashcroft & Mermin, we then perform a
 52 Taylor expansion:

$$f(x) = \sum_{m=0}^{\infty} \frac{1}{m!} (f^{(m)}(a) \cdot (x - a)^m) \quad (S4)$$

53 where $f^{(m)}(a)$ denotes the m^{th} derivative of the function $f(x)$, evaluated at $x = a$. For
 54 the right-most exponential term of $S(q, \omega)$, this expands to:

$$e^{\langle [q \cdot u(0)][q \cdot u(R, t)] \rangle} = \sum_m \frac{1}{m!} (\langle [q \cdot u(0)][q \cdot u(R, t)] \rangle)^m \quad (S5)$$

55 $m = 0$ represents zero-phonon processes, i.e., the scattering due to the lattice, and the
 56 Bragg reflections can be obtained, along with the Debye Waller factor, contributing to a
 57 smearing of the Bragg diffraction spots. The $m = 1$ term represents single-phonon scattering
 58 processes, for which we are interested. $m > 1$ terms represent multiple-phonon scattering
 59 processes, which we will neglect for now. Plugging the $m = 1$ term back into $S(q, \omega)$, we
 60 find:

$$S(q, \omega) = e^{-2W} \int \frac{1}{2\pi} e^{i\omega t} \sum_R e^{-iqR} \langle [q \cdot u(0)][q \cdot u(R, t)] \rangle dt \quad (S6)$$

61 If we limit ourselves to a single polarization p and reciprocal direction v analyzed at a
 62 single time, this eliminates the inner product. Also noting the relation to the Debye Waller
 63 factor:

$$\langle [q \cdot u(0)] \rangle^2 = 2W \quad (S7)$$

64 we find:

$$S(q, \omega) = e^{-2W} \int \frac{1}{2\pi} e^{i\omega t} \sum_R e^{-iq_v R_v} \sqrt{2W} q_v \cdot u_p(R, t) dt \quad (S8)$$

65 By eliminating scaling terms (including the q_v term outside the exponent) and rearranging
 66 slightly, we arrive at a nearly equivalent expression SED:

$$S(q, \omega) = \int \sum_R u_p(R, t) \cdot e^{i\omega t} e^{-iq_v R_v} dt \quad (S9)$$

67 which we compare to the expression used for SED for a single direction α sans scaling:

$$\Phi(\omega, k) = \int \sum_n v_{\alpha, n}(t) \cdot e^{i \cdot k \cdot \bar{r}_{\beta, n} - i \cdot \omega \cdot t} dt \quad (S10)$$

68 Differences lie in the use of velocities (v) for SED vs. displacements (u) for DNS, and
 69 the sign applied to the $i\omega t$ vs. $iq\bar{x}$ terms. The u vs. v can be accounted for via an ω scaling
 70 factor (based on $v = \frac{du}{dt}$; $u = e^{i\omega t}$, $v = i\omega e^{i\omega t}$), and the difference in sign merely indicates a
 71 difference in direction for the analyzed wave.

72 C. Comparing FRFPMS and TACAW

73 In the main manuscript, we stated that the two q-EELS simulations methods: FRFPMS
 74 developed by Zeiger *et al.* and TACAW developed by Castellanos-Reyes *et al.* [2], yield
 75 similar results. As a brief demonstration of this, we have included the parallel beam silicon
 76 dispersion and an energy slice for each in Figure S1. The apparently-higher resolution for
 77 FRFPMS is merely a product of the exceptionally-small frequency bin width, and results may
 78 vary. Our TACAW calculation is performed over 500 consecutive timesteps. Our FRFPMS

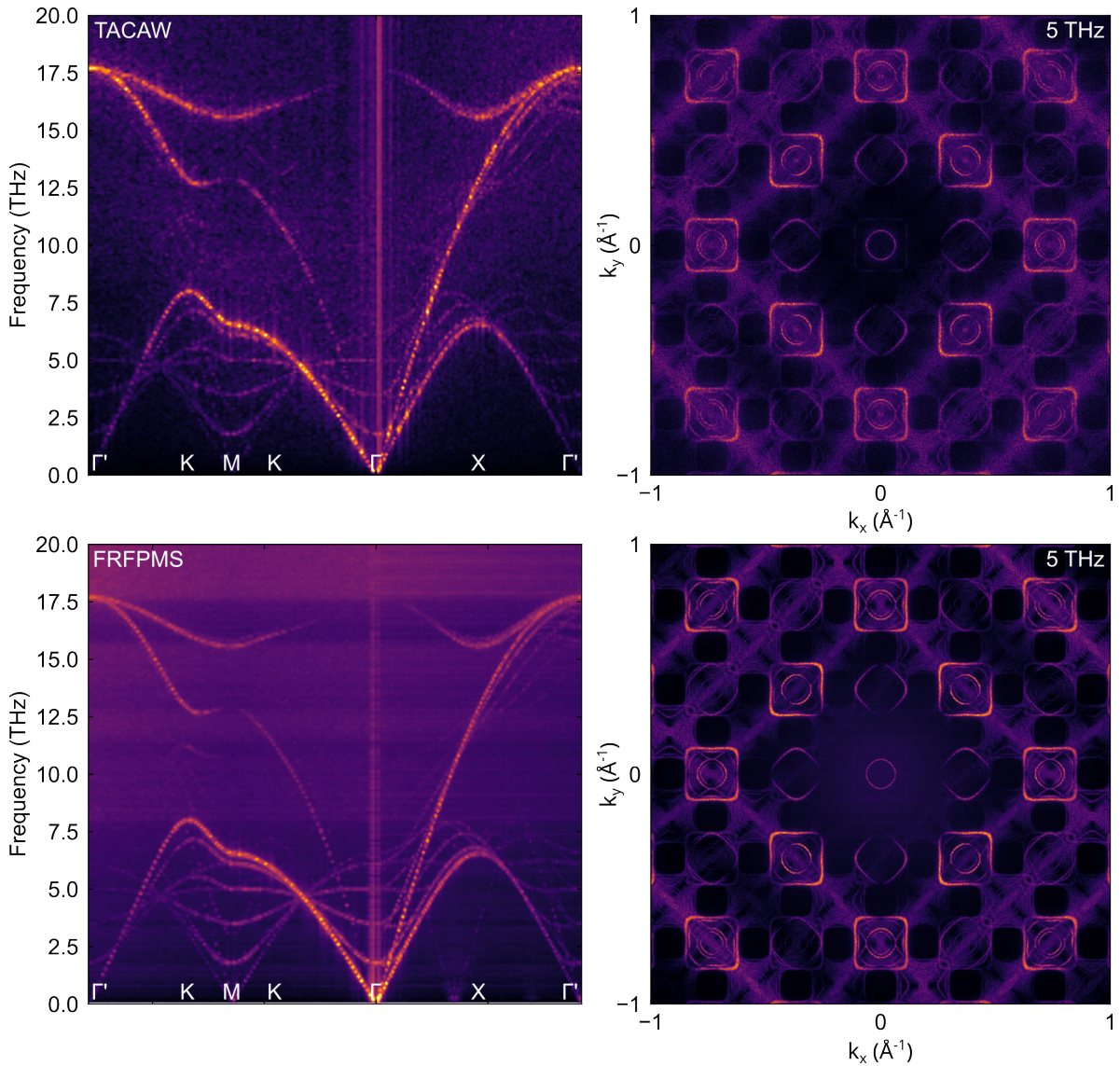


Figure S1. The two methods for q-EELS simulations are compared: FRFPMS developed by Zeiger *et al.* and TACAW developed by Castellanos-Reyes *et al.* [2]. All features in the data appear to be consistent regardless of which method is used

79 calculation was performed using 200 bins (every 0.1 THz, spanning a range of 20 THz), with
 80 a gaussian frequency filter width of 0.04 THz over 2000 timesteps. 20 randomized frozen
 81 phonon configurations were used for each frequency bin.

82 **D. Visualization of projected modes for finite thickness**

83 In the main manuscript, we highlight the presence of “phantom branches” which result
 84 from the projection of orthogonal waves onto the sampled direction. To further visualize

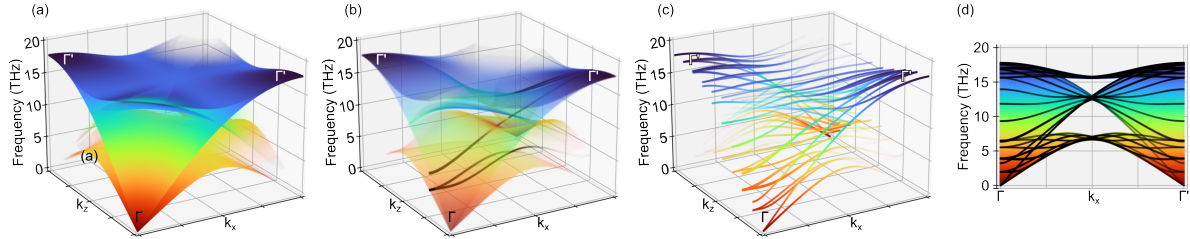


Figure S2. (a) To understand the source of the additional branches seen in the q-EELS simulations, we begin with the 3D phonon surface. (b) For a finite-thickness system, discrete slices across this surface represent the modes present. (c) The number of slices corresponds to the system size; here 10 slices are shown for a slab with a 10 primitive-cell thickness. (d) if these are projected into the Γ - X - Γ' direction (via non-uniform sampling of the waves), then the apparent wavevector of each is found, giving the appearance of additional branches.

85 this, we consider the 3D phonon dispersion surface seen in Figure S2, shown in Figure S2.a.
 86 For a finite-length system, this surface is not continuous and smooth, but rather there are
 87 a discrete number of k points along a given direction dependent on the size of the system.
 88 For a thin slab, we can approximate the surface as smooth in the semi-infinite direction, but
 89 discretized in the thickness direction. A single slice across this surface (at finite k_z , across all
 90 k_x) is shown in Figure S2.b. All slices of this surface are shown in Figure S2.c. Each point
 91 along these curves represents a wave in a low-symmetry direction, i.e., traveling orthogonal
 92 to the x direction. If these modes are projected onto Γ - X - Γ' (through uneven sampling of
 93 these orthogonal waves), the “side view” of this surface is found, shown in Figure S2.d.
 94

95 **E. q-EELS slices for silicon**

96 We have included the momentum-resolved diffraction images (or iso-energy phonon dis-
 97 persion surfaces) for Stillinger-Weber silicon, at 0.5 THz increments.

98 [1] Neil W. Ashcroft and N. David Mermin. *Solid State Physics*. Brooks Cole, 1 edition, January
 99 1976.
 100 [2] José Ángel Castellanos-Reyes, Paul M. Zeiger, and Ján Rusz. Dynamical theory of angle-
 101 resolved electron energy loss and gain spectroscopies of phonons and magnons in transmission

₁₀₂ electron microscopy including multiple scattering effects. *Phys. Rev. Lett.*, 134:036402, Jan
₁₀₃ 2025.

Figure S3. Energy-resolved diffraction images are shown for silicon for 0.5 THz increments, for a 0-20 THz range

